Evaluation of mixing and mixing rate in a multiple spouted bed by image processing technique

Yong Zhang,[1, 2] Wenqi Zhong,[*, 1] Xiao Rui,[1] Baosheng Jin,[1] Hao Liu[2]

[1]Key Laboratory of Energy Thermal Conversion and Control of Ministry of Education, School of Energy and Environment, Southeast University, Nanjing, 210096, China

[2]Faculty of Engineering, University of Nottingham, Nottingham NG7 2RD, UK

Abstract

Mixing efficiency is one of the most significant factors, affecting both performance and scale-up of a gas-solid reactor system. This paper presents an experimental investigation on the particle mixing in a multiple spouted bed. Image processing technique was used to extract the real-time information concerning the distribution of particle components (bed materials and tracer particles). A more accurate definition of the tracer concentration was developed to calculate the mixing index. According to the visual observation and image analysis, the mixing mechanism was revealed and the mixing rate was evaluated. Based on these results, the effects of operation parameters on the mixing rate were discussed in terms of the flow patterns. It is found that the detection of the pixel distribution of each component in RGB images is not affected by the interference of air void, thus maintaining good measurement accuracy.

*Corresponding author, Tel.: +86-25-83794744; Fax: +86-25-83795508.
E-mail address: wqzhong@seu.edu.cn

Convective transportation controls the particle mixing in the internal jet and spout, while shear dominants the particle mixing in the dense moving region. Global mixing takes place only when the path from one spout cell to the other is open. This path can be formed either by the bubbles or particle circulation flows. The mixing rate is linked to the bubble motion and particle circulation. Provided that there are interactions between the spout cells, any parameters promoting the bubble motion and circulation can increase the mixing rate. Finally, a mixing pattern diagram was constructed to establish the connection between the flow structure and mixing intensity.

Keywords: particle mixing; mixing rate; multiple-spouted bed; flow regime; mixing pattern map

1 Introduction

Spouted bed technology has proven to be a suitable technology for physical and chemical operations that require handling solids with large particle size, irregular texture and sticky nature due to its inherent advantages of smooth cyclic movement of the particles and efficient fluid-solid contact [1-9]. However, spouted bed is likely to operate in unsteady and non-optimal modes when the vessel diameter is larger than 1 m, which limits the scale-up of spouted bed in its practical applications [10]. In order to achieve the optimum performance and facilitate the scale-up of spouted bed, some modifications have been promoted, including the spout-fluid bed, slot-rectangular spouted bed and multiple-spouted bed. For industry applications, the multiple-spouted bed which divides the overall system into modular spouted beds in parallel is one of the valuable and preferred modifications to spouted bed [10].

Although a number of experimental and theoretical studies have been performed on the hydrodynamic features for spouted bed over past decades, only a few studies have been focused on the multiple-spouted beds. Murthy et al. [11] measured the minimum spouting velocity in three rectangular columns having 2, 3 and 4 spout cells and found that the number of spout cells has no effect on the minimum spouting velocity. In addition to the minimum spouting velocity, Zhang et al. [12] investigated the maximum spouted pressure drop and the maximum spoutable height in a double-nozzle spouted bed. In their work, the minimum spouting velocity was found to increase with the particle diameter and the distance between two nozzles. For the flow pattern, Murthy et al. [13] plotted the phase diagrams and identified five flow

regimes in multiple spouted beds having 2, 3 and 4 spout cells. Previously we also conducted experimental study on the flow patterns and transitions in a multiple-spouted bed [14]. Regarding the classification of flow patterns, we developed the classification criteria, the schematic diagrams and obtained the typical flow pattern images by a digital CCD camera. Different flow patterns can lead to different mixing behaviors and mixing mechanisms, but this was not investigated in our previous work [14]. In a flat bottom spouted bed with 7 spouts, Foong et al. [15] performed some particle mixing experiments and found that there was 12.8 vol% dead zones existing in the bed. Saidutta et al. [16] used the 'spout mixing number' to explain the extent of mixing flow volume in a continuously operated multiple spouted bed. To enhance particle flow and eliminate stagnation in the annular space, Hu et al. [17, 18] proposed a novel multiple-nozzle spouted bed and investigated the spoutable bed height, flow pattern and particle mixing characteristics.

In recent years, numerical simulation as a useful tool has been widely used for studying the hydrodynamic characteristics of gas-solid systems including spouted beds. Li et al. [19] simulated the flow patterns in a multiple-spouted bed with mono-dispersed particles adopting the two-fluid Eulerian model and investigated the effects of the hydrodynamic parameters on the flow patterns. By means of the discrete particle model (DPM), Maureen et al. [20] investigated the influence of multiple spouts on the bed dynamics in a triple-spout fluidized bed and used the positron emission particle tracking (PEPT) measurements for the validation of their modeling results.

Partly due to the lack of full knowledge on the flow characteristics, the industry applications of the multiple-spouted bed are still limited. As one of the most important hydrodynamic characteristics, the particle mixing characteristics play an essential role in designing and operating multiple-spouted bed reactors. Particle mixing directly influences the rates of mass, heat and moment transfers among reactants and products [21]. Furthermore, good mixing is essential to avoid temperature hot spots due to the heat released by exothermic reactions, whereas bad mixing can result in coking and agglomeration, further lowering the overall process efficiency and complicating its thermal control [22]. There are a number of knowledge gaps regarding the particle mixing with a multiple-spouted bed reactor. For example, how will the new feed materials disperse across the reactor's cross-sectional area and mix with the existing bed materials? How long will it take for the new feed materials to completely mix with the existing bed materials? What is the relationship between the operating condition and particle mixing behavior?

In order to enhance our understanding and fill some of the existing knowledge gaps on the particle mixing within a multiple-spouted bed, an experimental investigation focusing on the particle mixing behavior and mixing rate has been carried out in the same multiple-spouted bed used with our previous work which focused on the investigation of flow patterns [14]. In this study, particular emphasis was given to the mixing rate, which was indicated by the mixing time required to achieve a given mixing index of the tracer particles. The auxiliary and central spouting gas flow rates were adjusted to cover a wide range of flow regimes. The mixing behavior was

analyzed in terms of the particle concentration profile and flow regimes. In order to establish the connection between the operating condition and the mixing rate, the particle mixing pattern map was plotted on the basis of the flow regime map and the corresponding snapshots.

2 Experimental section

2.1 Experimental setup

The experiments were carried out in the multiple spouted bed with a rectangular cross-section of 300 mm × 30 mm and a height of 1200 mm. The entire device is constructed of acrylic glass plates, which enables visual observation and recording of the flow and mixing. The multiple spouted bed can be regarded as the combination of three spouted bed cells with a cross-section of 100 mm×30 mm, each has an independent spout nozzle with a cross-section of 10 mm×30 mm. Further details of the experimental setup have been reported in our previous work [14].

2.2 Materials

The bed materials used in this study are polypropylene beans with a mean diameter of 2.8 mm and real density of 900 kg/m^3. Its minimum fluidizing velocity is 0.82 m/s. The tracer particles used in this investigation were prepared by coloring the same bed materials as those in the multiple spouted bed with direct dyes. So the tracer particles share the identical physical properties with the bed materials except the color. This method was successfully used in our previous study on the particle mixing in a spout-fluid bed [23].

2.3 Experimental method

All the mixing experiments were performed in batches at room temperature and atmospheric pressure. At the beginning of each test, the bed materials were first poured into the bed from the gas outlet, and some tracer particles were carefully placed at the same location for each test. All experiments were carried out with the mass of tracer particles accounting for about 7.1% of the total particles mass. After the above preparation, the auxiliary and central spouting gas flow rates were adjusted to desired values, respectively. During each run, the bed was illuminated by two 2000 W floodlights, one on each side for uniform lighting. Thus, the mixing process could be continuously captured by a digital video camera. All the pictures were recorded in the RGB (Red, Green and Blue) format and transmitted into the computer for further image processing.

In this study, we characterize the mixing degree of bed materials and tracers in a multiple spouted bed by the optical properties. In the digital imaging, a pixel is the smallest controllable element of a picture, which records much digital information. For example, the address of a pixel indicates its physical coordinates, and the intensity of each pixel represents its local color. The specific color that the intensity of a pixel describes is a blend of three components of the color spectrum - RGB. Generally, the intensity of pixel is designated by three values ranged from 0 to 255, corresponding to red, green and blue components. So through scanning the picture, one can obtain the distribution of every component with different colors.

Considering that there is a great deal of images taken successively for one run, a

batch-processing algorithm was developed to implement repetitive processing and calculations in series for a set of images. A flow chart describing the batch processing procedure is shown in Figure 1, which also includes a real image as an example. The first step is to pre-process the original image. An original image is first read and cut to remove redundant parts. Image enhancement is then performed to adjust image's brightness and contrast. This process is accomplished with the help of the Adobe Photoshop CS2 image processing program. The second step is the image analysis. The detection of RGB range of a single tracer particle is first done. After that, to identify the distribution of tracer component, a range of threshold values are set. Thus, based on the comparison of thresholds and intensities, the distribution of tracer particles is automatically decomposed and reconstructed against the black background, as shown in Figure 1b. Then, the interested region is subdivided into many segments that correspond to a sample cell size of w mm$\times$$h$ mm. Within each segments, the total area occupied by the tracer particles is easily determined by accounting the number of pixel points, as shown in Figure 1d. The same procedure is used for the detection of bed materials. The above-mentioned process is accomplished by the Image Processing Toolbox of MATLAB software. The last step is to calculate the tracer concentration by using Microsoft Excel worksheet.

As for the tracer concentration, it can be measured using box-counting method whose principle is to count the number of particles inside the box (sample cell). The same method was also used in our previous work which investigated the particle mixing in a spout-fluid bed [23]. Here, the area occupied by particles represents the

number of particles. So, the tracer concentration is defined as the ratio of the area occupied with the tracer particles detected within a given sample cell to the total area covered by both tracer particles and bed materials. Shen [24] had used the same method to investigate the biomass mixing in a fluidized bed. Since their bed material particle size was very small, only equal to several pixels, they treated all particles (bed materials and biomass particles) as one component. Therefore, the area of their sample cell represents the total area covered by both biomass and bed material particles in their definition of particle concentration. This may cause error especially when considering the total area of the sample cell is not only occupied by biomass particles and bed materials, but also by the gas bubbles.

Image processing method can follow the homogeneity of the mixture without interrupting the mixing process and does not need any sample preparation. However, it should be mentioned that due to the bed thickness, a fraction of tracers will be covered by the bed materials and not present near the front wall of the bed. Considering the stochastic process of particle mixing, the probability of appearance of the tracer along the direction of the bed thickness should be constant. Therefore, it is reasonable to consider the near wall region as representative of the whole bed.

Figure 2 depicts the size and location of the spout cells and sample cells in the bed. The size of a sample cell is indicated by w mm$\times$$h$ mm. The position of a sample cell is indicated by its dimensionless coordinate or serial numbers. So the sample cell with the green color in Figure 2 is located at distances of y/h_0 above the bottom wall and x/w_0 from the left wall. Here, h_0 is the height of fixed bed and w_0 is the width of the

bed. Alternatively, it can be indicated as $SC_{(column,\ row)}$=$SC_{(3,\ 5)}$. The tracer particles were placed on the right side of the bed covering eight sample cells to simulate the inlet of the bed material.

In the present work, a dimensionless index *M* is used to characterize the degree of mixing, which is given by:

$$M = \frac{\sigma(c)}{\bar{c}} \tag{1}$$

Here $\sigma(c)$ is the standard deviation of tracer concentration, which can be calculated by:

$$\sigma(c) = \sqrt{\frac{\sum_{i=1}^{m}\sum_{i=1}^{n}(c_{i,j} - \bar{c})^2}{k-1}} \tag{2}$$

where *k* is the number of sample cells, $\bar{c}$ is the mean concentration of tracer in the whole bed and $c_{i,j}$ is the tracer concentration in the sample cell of $SC_{(i,j)}$. So the value of *M* close to zero means a homogeneous distribution of tracers. And a higher value of *M* indicates a larger degree of inhomogeneity.

The size of the sample cells can have a significant influence on the quality of mixing defined above. In fact, there is a greater probability of measuring a better degree of mixing with larger sample cells because the mixing quality is related to the global concentration as well. In theory, the smallest cell size is at the size of the particles. This leads to the question of what size of sample cells should be selected. In the present work, the sample cell size is determined based on the balance between the accuracy of *M* value and the time consumed with the data processing. By comparing the mixing index of five various scales of sample cells with 75 mm×75 mm, 50 mm ×50 mm, 30 mm×30 mm, 20 mm×20 mm and 15 mm×15 mm, one can find that

the measured mixing index became higher with the reduction of the cell size from 75 mm×75 mm to 30 mm×30 mm, while it remained almost the same when the cell size was 20 mm×20 mm and 15 mm×15 mm. However, the number of images for the cell size of 15 mm×15 mm was 66.7% higher than that of the cell size of 20 mm ×20 mm, and hence required much longer time to process the data. Therefore, the cell size of 20 mm×20 mm is considered to be appropriate as it leads to a good accuracy in the measured mixing degree and does not require excessively long time for data processing. The results presented below were obtained using a sample cell of 20 mm in width and 20 mm in height.

The process of particle mixing in a multiple spouted bed is somewhat stochastic, especially at the bubbling zone. To investigate whether the measured tracer concentrations are representative, ten repeated runs were carried out under a fixed operation condition. Figure 3 presents the tracer concentration profiles with error bar for the ten repeating runs. It also displays the comparison of the averaged value calculated by the method of this study with those obtained by means of literature method [24]. Figure 3 clearly shows the measured tracer concentrations are well repeatable. The maximal error of the measured tracer concentration between repeating runs was below 5.8%. Figure 3 also shows that almost all of the averaged tracer concentrations calculated by the literature method [24] are lower than those calculated using the proposed method of the current work. This further verifies that the area covered by the tracers and bed materials is not equal to the area of the sample cell as assumed by Shen et al. [24].

3 Results and discussions

3.1 Flow structures

The flow structure exerts a profound impact on the mixing behavior of solids. During the transient state of the particulate flow, the main stage of mixing tends to take place. Therefore, the flow structure should be first investigated to understand the mixing behavior and mechanism. In our previous work [14], four representative flow patterns were identified and illustrated, which are internal jet (IJ), internal jet with bubble (IJB), single spouting (SS) and multi-spouting (MS). These representative flow patterns were again confirmed in the present study (Figure 4).

When the bed is operated at the stage of IJ, the jet profile exhibits three typical structures: isolated, transitional and interacting, which is dependent on the respective jet velocities. In Figure 4a, isolated jet structures can be observed where there is no particle transport occurring between the adjacent jet moving regions. While in the structure of interacting jet, it is seen from in Figure 4c that the central jet region interferes with two auxiliary jet regions. Obviously, the structure of transitional jets is between the isolated and interacting jets. As witnessed from Figure 4b, the right jet behaves as an isolated one while the central jet region only interacts with the left one.

At the flow regime of IJB, bubbles lifting off the top of neighboring jets coalesce into one relatively big bubble, ultimately breaking up at the bed surface. So in this case, only transitional and interacting jet profiles can be seen. The former is characterized by the predominant generation of big bubbles at the one side of the bed, as illustrated in Figures 4d and 4e. The latter can be found that big bubbles emerge

randomly and move at the upper part of the bed (Figure 4f), greatly improving the horizontal movement of particles.

If one of three jet velocities exceeds the minimum spouting gas velocity, the single spouting will take place. This flow structure distinctly differs from that in a conventional spouted bed. The main difference lies in the appearance and stability of spout region, depending on the fountain structure and neighboring jet velocity. When the fountain in the spout cell 1 or 3 is over-developed and the other jet regions interact with the moving region, the dissymmetrical spouting is most likely to occur, as shown in Figure 4g and 4h. This attributes to the combined influence of the extrusion of left lower moving region and the oppression of right upper moving region. If the spouting is formed in the spout cell 2 (in Figure 4i) under the interaction of surrounding jets, the spout region periodically swings from one side to the other. This is due to the fact that the two auxiliary jets swing toward the central spout region in turn because of the entrainment of the central jet.

Once the multi-spouting takes place, two or three distinct fountains can be observed. In this case, two auxiliary fountains and moving regions can interact with the central fountain and moving region, as shown in Figure 4j. Alternatively, two auxiliary fountains and moving regions are able to interact with each other, as shown in Figure 4k and 4l. On the condition of Figure 4k, the central jet region is isolated. While in this case of Figure 4l, the development of central jet will be successively suppressed by the top moving regions. Thus, it shows the signs of bending towards the one side. This flow pattern has a potential advantage for the particle mixing in three spout cells.

3.2 Distribution of tracer concentration

To assist discussion, three spouting gas flow rates are expressed as dimensionless parameters, given by:

$$Q_{a1}^{*}=Q_{a1}/Q_{mf} \quad (3)$$

$$Q_{a2}^{*}=Q_{a2}/Q_{mf} \quad (4)$$

$$Q_{c}^{*}=Q_{c}/Q_{mf} \quad (5)$$

in which Q_{a1} and Q_{a2} are the gas flow rate through the nozzles of the spout cell 1 and 3, respectively; Q_c is the gas flow rate through the nozzle of the spout cell 2; Q_{mf} is the minimum fluidizing gas flow rate of the whole bed. Comparing with individual spouting gas flow rates, these dimensionless numbers are the fundamental parameters more useful for the scale up of the industry reactors [10].

Figure 5 displays the axial distribution of tracer concentration at the mixing time t=30s with different operating parameters. It should be noted that t=30s was only taken as an illustration example to discuss the distribution of the particle concentration at a given moment. At t=0, the tracer particles were always placed in the spout cell 3. It is obvious that three profiles of the tracer concentration follow the same trend. That is, the curves at three spout cells become flatter with increases in spouting gas flow rates. But in various spout cells, there exists an obvious difference in the variance of the tracer concentration. Under the first set of test conditions (Q_{a2}^{*}=1.33, Q_{c}^{*}=0.40 and Q_{a2}^{*}=0.67), the measured tracer concentration in the spout cell 1 was equal to zero along the bed height, implying that tracer particles were still limited to the initial spout cell 3. Then, when Q_{a2}^{*} was increased to 1.42, the tracer

concentration in the spout cell 1 showed an increasing trend, evidencing that tracers gradually moved into the spout cell 1. This may be due to the interaction and coalescence of neighbouring bubbles at the upper bed, which creates one channel for tracers to enter into the spout cell 1. Furthermore, the tracer concentration at the upper part of the bed was far higher than that at the lower part. This is because that a downflow of tracers first existed in the upper region surrounding the central jet. It can also be observed that further increase in the auxiliary and/or central gas flow rate make the profiles of the tracer concentration along the bed height flatter.

It can be seen from Figure 5b that even that Q_{a2}^* was increased to 1.42, the value of the tracer concentration in the lower region of the bed in Cell 2 remained at zero. This suggests that there is not enough driving force for the jet region in the spout cell 2 to interact with other regions. For practical operations, freshly fed materials from Cell 3 would have no opportunity to be delivered to the lower region. There are two recommended ways to deal with this problem. One is to increase the flow rate of the other auxiliary spouting gas and the other is to increase the flow rate of the central spouting gas. In Figure 5, the condition of Q_{a1}^*=1.33, Q_c^*=0.4 and Q_{a2}^*=2.39 represents the first way, whereas the case of Q_{a1}^*=1.33, Q_c^*=0.79 and Q_{a2}^*=2.39 represents the second recommended way. It can be seen that both conditions led to increases in the tracer concentration in the lower region of the bed in Cell 2.

Since more tracer particles were transported from the spout cell 3 to spout cell 2 and 1 with an increase in the gas flow rate Q_{a2}^*, the concentration of tracer particles in the spout cell 3 decreased accordingly. This can be verified from Figure 5c where

almost all of the tracer concentration values along the bed level were getting smaller with the increase in the gas flow rates Q_c^* and Q_{a2}^*.

Figure 6 shows the lateral distribution of the tracer concentration at t=30s with different operating parameters. It is interesting to note that the tracer concentration on the right side is higher than that on the left side of each spout cell, especially at low gas flow rate. This can be explained as follows. Before the jet in the spout cell 3 penetrated the bed, the particle exchange between different spout cells was induced by the motion of bubbles, especially when the bubbles merged. Under this condition, bubbles had a trend to migrate toward the bed centre, which led to the nonuniform distribution of tracers. Once the spout broke through the bed surface, the moving region induced by the spout extended to the upper part of spout cell 2. The moving region had a shape of inverted triangle, which contributed to the uneven distribution of the tracer concentration. The interaction of bubbles with the moving region promoted the transportation of tracers from the spout cell 3 to 1. On the whole, the increase in gas flow rate helped to achieve a good mixing degree within a shorter time.

3.3 Identification of mixing mechanism

On the basis of the visual observations and concentration profiles, we can identify three types of motion patterns for particles in different spout cells. As illustrated in Figure 7, they are: (1) bubble-induced motion—which principally takes place on the top of jet and is mainly induced by the bubble motion, including the coalescence and breakup of bubbles. This motion is similar to that of bubbling fluidized bed. (2)

jet-induced motion—which is caused by an upward-flowing gas stream into the fixed bed. This movement pattern is exhibited in the form of particle circulation, including the internal circulation occurring in the internal jet and external circulation happening in the spout. (3) bubble-jet cooperative motion—which is due to the interaction of bubbles with the moving region as a part of the particle circulation.

Correspondingly, these motion patterns give rise to three underlying mechanisms of particle mixing: convective, diffusive and shear mixing. In the case of convective mixing, particles are transported from one location to another. Obviously, the bubble and jet are the driving force for convective mixing. While shear mixing occurs at the area where two groups of particles moving at differing speeds contact each other. This mixing mechanism plays a major role in the dense moving region. Diffusive mixing means the random motion of individual particles through the gaps among particles. So this mixing mechanism mainly occurs in the dilute spout and fountain, especially when two or three spout regions merge into one spout and multiple fountains interact with each other.

These mixing mechanisms tend to occur simultaneously in a real multiple spouted with the dominant mechanism depending to a great deal on the operation condition. For example, when two bubbles generated at the top of the respective jets merge into one large bubble and break up at the surface of the bed, the bubble-induced convective mixing takes place. This leads to particle mixing in various bed cells, as shown in Figure 7b. When the single spout is formed in the spout cell 2 (Figure 7c), bubbles generated at the auxiliary jets lead to the convective mixing between the

moving region and the jet region. Due to the interference of the auxiliary jets, the moving region suffers a deformation, leading to the shear mixing (Figure 7c). If the triple spouts form (Figure 7f), the mixing happens as a result of all three mixing mechanisms. Shear mixing happens at the interface of adjacent moving regions, while diffusive mixing occurs in the interaction of neighbor fountains. Once two jets combines into one spout, shear mixing also occurs at the interface of adjacent moving regions, as shown in Figure 7g.

3.4 Variation in the mixing time

Figure 8 shows two typical plots of mixing index fluctuations as a function of time at different operating parameters (case one Q_{a1}^{*}=1.12, Q_{c}^{*}=0.43, Q_{a2}^{*}=0.62 and case two Q_{a1}^{*}=2.25, Q_{c}^{*}=0.43, Q_{a2}^{*}=1.96). It shows for both cases that as the mixing proceeds, the mixing index gradually decreases until an equilibrium state of mixing is reached. This implies that the mixing significantly improves with time. However, the mixing indexes at the mixing equilibrium is extremely different with case 1 having much higher equilibrium mixing index value than case 2. This suggests that the latter (case 2) achieves better mixing quality. Furthermore, it can also be noted that the mixing time t_e increases from 48.1s with case 1 to 91.9s with case 2. Here, the mixing time t_e is defined as the time span necessary to reach the homogeneity at the equilibrium state. That is to say, the mixing rate for the case 1 is higher than that for the case 2. This can be explained by the fact that the jet region with case 1 was isolated and the mixing between tracer particles and bed materials was only limited within the spout cell 3. While with case 2, the flow pattern of double spouting forms and the fountain in the

spout cell 3 directly interacts with the fountain in the spout cell 1. As a result, more tracer particles in the spout cell 3 are agitated and move into the spout cell 1. So this will take a lot of time for tracer particles to become homogenously mixed with the bed materials in spout cells.

In order to correlate the mixing time with operating conditions, one dimensionless parameter is defined as below:

$$t^*=t_e/t_{mf} \tag{6}$$

where t_{mf} is the elapsed time for gas to flow through the whole bed at the minimum fluidization state. So t^* can be used to compare the mixing rate under different operation conditions.

The dimensionless mixing time, t^*, is plotted against Q_c^* in Figure 9. It should be noted that the bed was started from three isolated jets at Q_{a1}^*=0.51, Q_c^*=0.48 and Q_{a2}^*=0.81. As can be observed from Figure 9, the initial increase in Q_c^* from 0.5 to 0.75 had little effect on t^*. But a further increase of Q_c^* to 1.0 caused t^* to sharply jumps to a high value. Since the initial increase of gas velocity failed to change the flow structure of three isolated jets, the mixing in the spout cell 3 was independent on the central spout gas.

But it would be different once the path for tracer particles moving from the spout cell 3 to cell 2 had been opened by bubbles. This led to the mixing of particles on the top of jets and hence the sudden enhancement of t^*. After that, further increasing Q_c^* from 1.0 to 1.25 promoted the diffusive mixing induced by bubbles, leading to the observed small decrease in t^*. When Q_c^* was increased to 1.61, the moving region

induced by the central jet not only extended to the spout cell 1 but also interacted with the jet region there. As a result, tracer particles also entered into spout cell 1 and hence it would take a lot of time for them to be homogenously mixed in spout cell 1. Further increases in Q_c^* resulted in the gradual reduction of the mixing time. This phenomenon can be explained by the following facts. Firstly, higher Q_c^* accelerated the convective mixing due to the increase in circulation rates. Secondly, the spread of moving region strengthened the shear mixing because of the improvement in its interaction with the other two jet regions.

Figure 10 shows the effect of the auxiliary spouting gas flow rate on the dimensionless mixing time. When Q^*_{a1} was increased from 0.65 to 0.89, a similar trend as described above was also observed. That is, the initial increase in Q_c^* had little effect on t^*. A further increase in Q^*_{a1} to 1.36 caused the significant increase of the mixing time as the region of mixing expands as a result of the jet regions interacting with each other. Here, it should be emphasized that the region of mixing indicates the region where the mixing between tracer particles and bed materials takes place. Further increases in Q^*_{a1} reduced the mixing time within the same region of mixing.

3.5 Flow regime and mixing pattern map

For the current multiple-spouted bed, the interaction of jet/spout gives rise to distinctive flow patterns, which can be distinguished both by visual observation and pressure drop measurements. Figure 11 displays a typical flow regime diagram with the dimensionless central spouting gas flow rate Q_c^* plotted on the abscissa axis and

the dimensionless auxiliary spouting gas flow rate Q_{a1}*(=Q_{a2}*) plotted on the ordinate. It should be emphasized that this flow regime has been presented in our previous work [14].

On the flow regime map, we have added the mixing rate (in terms of dimensionless mixing time t*) with different colors to form the new flow regime and mixing rate map. This new map establishes the connection between the flow regime and mixing behavior in the multiple-spouted bed.

Figure 11 clearly shows that t* varies with the flow regimes. By keeping Q_c* constant and changing Q_{a1}*(=Q_{a2}*), one can obtain a desired mixing rate. For example, when the multiple-spouted bed is operated at Q_c*=0.45 and Q_{a1}*(=Q_{a2}*)=0.93 (in the flow regime of IJ), a gradual increase of Q_{a1}*(=Q_{a2}*) will lead to the initial increase and then decrease of t*. When Q_c* is kept 1.24 and Q_{a1}*(=Q_{a2}*) is increased from 0.33 to 2.98 in which the flow regime is transferred from IJ to MS, t* first increases and reaches the maximum in the vicinity of the boundary between two regimes, then decreases slowly. When the operation condition is Q_c*= 2.37 and Q_{a1}*(=Q_{a2}*)=0.6 (in the case of SS), the increasing Q_{a1}*(=Q_{a2}*) will result in the continue decrease of t*. By keeping Q_{a1}*(=Q_{a2}*) constant and adjusting Q_c*, we can obtain a desired mixing rate. For example, in the case of low auxiliary spouting gas flow rate (e.g. Q_{a1}*(=Q_{a2}*)= 0.65), with increasing the central spouting gas flow rate, the flow regime transits from IJ to IJB and then to SS, which leads to the initial increase and then decrease of t*. When the auxiliary spouting gas flow rate is relatively high (Q_{a1}*(=Q_{a2}*)= 1.47), the transition of flow regime from IJB to SS

will cause t^* to constantly decrease.

Figure 11 also shows that even the bed is operated at the same flow regime, the mixing rate is different. In some regimes, the span of t^* is quite lager. For example, at the flow regime of IJ, the maximum t^* is located between 14-16, while the minimum t^* is lower than 4. This can be explained by the fact that for the former the particle mixing takes place in more than one spout cell, whereas for the latter the particle mixing only occurs in one spout cell. In some regions, the span of mixing time (t^*) is quite small. For example, at the flow regime of MS, most of t^* values are lower than 4. This can be contributed to the fact that there are at least two regions in which the spouting occurs. Most importantly, the formed fountain tends to interact with each other.

The new flow regime and mixing map can provide useful guidance for a practical multi-spouted bed chemical reactor. For example, to achieve a quick mixing with the freshly added materials (represented by the tracer particles), we should choose the flow regime of MS or SS at high Q_c^*, in which good mixing can be achieved in a very short time. On the other hand, in order to achieve a longer residence time with the reactant particles (represented by the tracer particles) in the bed, we can adjust the operation parameter (Q_c^* or Q_{a1}^*/ Q_{a2}^*) to ensure that the bed is operated at the flow regime of IJB or partial IJ.

4 Conclusions

Particle mixing characteristics have been studied in a multiple spouted bed having

three spout cells. The mixing rate was evaluated using image processing technique. The mechanism of mixing was revealed by use of combined visual observation and digital image analysis. Further, the effects of central and auxiliary spouting gas flow rate on the mixing rate were discussed in terms of the flow patterns. The key findings are as follows:

(1) The air void in RGB images can be excluded by individually detecting the pixel distribution of each component, thus maintaining good measurement accuracy. The developed algorithm for imaging processing makes it possible to automatically obtain the tracer concentrations in all sample cells which are then used to calculate the mixing index. The image processing method is successfully performed to evaluate the mixing rate in a multiple spouted bed.

(2) Three motion patterns, jet-induced, bubble-induced and bubble-jet cooperative motion, can be determined in a multiple spouted bed. They lead to three mixing mechanisms: convective, diffusive and shear. Convective transportation controls the particle mixing in the internal jet and spout, while shear dominants the particle mixing in the dense moving region. Diffusive mixing mainly occurs in the dilute spouts and fountain regions.

(3) Local mixing occurs if the particle motion is only limited into an isolated spout cell. While global mixing takes place only when the path from one spout cell to the other is open. This path can be formed either by the bubbles or particle circulation flows. The bubbles tend to predominate at the internal jet with bubble, and particle circulation flows at the multi-spouting.

(4) The particle mixing rate is closely related to the bubble motion and particle circulation. Provided that there are interactions between the spout cells, any parameters promoting the bubble motion and circulation can increase the mixing rate. In addition, the interaction of bubbles with moving regions causes the deformation of the latter, thus improving the shear mixing.

(5) The new mixing pattern diagram has been constructed to establish the connection between the flow structure and mixing intensity. It can also provide useful guidance for a practical multi-spouted bed chemical reactor. For example, to achieve a quick mixing with the freshly added materials or a longer residence time with the reactant particles in the bed, one can choose different mixing regimes by adjusting the flow rate of central to auxiliary spouting gas.

Acknowledgement

The authors gratefully acknowledge financial support from the National Natural Science Foundation of China (Grant No. 51390492, 91334205), A Foundation for the Author of National Excellent Doctoral Dissertation of PR China (201440) and Teaching and Research Fund for Outstanding Young Teachers in Southeast University (2242015R30004). The authors also acknowledge the provision of a scholarship to Yong Zhang by the China Scholarship Council (CSC) that enabled him to carry out part of the reported work at the University of Nottingham.

References

[1] Mathur KB and Epstein N, 1974. Spouted Beds. Academic Press, New York.

[2] San José MJ, Olazar M, Izquierdo MA, Alvarez S and Bilbao J. Solid trajectories and cycle times in spouted beds. Ind Eng Chem Res 2004; 43: 3433-3438.

[3] Lim CJ, Watkinson AP, Khoe GK, Low S, Epstein N and Grace JR. Spouted, Fluidized and spout-fluid bed combustion of bituminous coals. Fuel 1988; 67: 1211-1217.

[4] Aguado R, Olazar M, San Jose´MJ, Aguirre G and Bilbao J. Pyrolysis of sawdust in a conical spouted bed reactor. yields and product composition. Ind Eng Chem Res 2000; 39: 1925-1933.

[5] Olazar M, Aguado R, Barona A and Bilbao J. Pyrolysis of sawdust in a conical spouted bed reactor with a HZSM-5 catalyst. AIChE J 2000; 46: 1025-1033.

[6] Aguado R, Olazar M, Gaisa´n B, Prieto R and Bilbao J. Kinetic study of polyolefins pyrolysis in a conical spouted bed reactor. Ind Eng Chem Res 2002; 41: 4559-4566.

[7] Aguado R, Olazar M, San Jose´ MJ, Gaisa´n B and Bilbao J. Wax formation in the pyrolysis of polyolefins in a conical spouted bed reactor. Energ Fue. 2002; 16: 1429-1437.

[8] Olazar M, San Jose´ MJ, Zabala G and Bilbao J. A new reactor in jet spouted bed regime for catalytic polymerizations. Chem Eng Sci 1994; 49: 4579-4588.

[9] Olazar M, Arandes JM, Zabala G, Aguayo AT and Bilbao J. Design and simulation of a catalytic polymerization reactor in dilute spouted bed regime. Ind

Eng Chem Res 1997; 36: 1637-1643.

[10] Epstein N and Grace JR, 2011. Spouted and spout-fluid Beds. Cambridge: Cambridge University Press.

[11] Murthy DVR and Singh PN. Minimum spouting velocity in multiple spouted beds. Can J Chem Eng 1994; 72: 235-239.

[12] Zhang SF, Wang SH and Zhao JB. Experimental study on hydrodynamics characteristics of dobble-nozzle rectangular spouted bed. Chem Eng 2006; 34: 33-39.

[13] Murthy DV R and Singh PN, 1996. Minimum spouting velocity in multiple spouted beds, in mixed-flow hydrodynamics: advances in fluid mechanics series, Nicholas P. Cheremisinoff, Ed., Gulf Publishing Company, Houston, TX . pp. 741-758.

[14] Ren B, Zhong WQ, Zhang Y, Jin BS, Wang XF, Tao H and Xiao R. Investigation on flow patterns and transitions in a multiple-spouted bed. Energ. Fuel 2010; 24: 1941-1947.

[15] Foong SK, Barton RK and Ratcliffe JB. Characteristics of multiple spouted beds. Mech and Chem Trans Ins. Eng 1975; 7-12.

[16] Saidutta MB and Murthy DVR. Mixing behaviour of solids in multiple spouted beds. Can J Chem Eng 2000; 78: 382-385.

[17] Hu GX, Gong XW, Wei BN and Li YH. Flow patterns and transitions of a novel annular spouted bed with multiple air nozzles. Ind Eng Chem Res 2008; 47: 9759-9766.

[18] Huang H and Hu GX. Mixing characteristics of a novel annular spouted bed with several angled air nozzles. Ind Eng Chem Res. 2007; 46: 8248-8254.

[19] Li YC, Che DF and Liu YH. CFD simulation of hydrodynamics in a multiple-spouted bed. Chem Eng Sci 2012; 80: 365-379.

[20] van Buijtenen MS, van Dijk WJ, Deen NG and Kuipers JAM. Numerical and experimental study on multiple-spout fluidized beds. Chem Eng Sci 2011; 66: 2368-2376.

[21] Zhang Y, Jin BS and Zhong WQ. Experimental investigations on the effect of the tracer location on mixing in a spout-fluid bed. Ind J Chem Res Eng 2008; 6: 1-20.

[22] Zhang Y, Zhong WQ, Jin BS and Xiao R. Mixing and segregation behavior in a spout-fluid bed: effect of particle size. Ind Eng Chem Res 2012; 51: 14247-14257.

[23] Zhang Y, Jin BS and Zhong WQ. Experiment on particle mixing in flat-bottom spout-fluid bed. Chem Eng Process 2009; 48: 126-134.

[24] Shen LH, Xiao J, Niklasson F and Filip J. Biomass mixing in a fluidized bed biomass gasifier for hydrogen production. Chem Eng Sci 2007; 62: 636-643.

Figure captions

Figure 1 Flow chart of an image batch processing algorithm for calculating tracer concentration of a series of images. (a) original image; (b) detected tracers against the black background; (c) detected bed materials against the black background; (d) sample cell division for tracers; (e) sample cell division for bed materials.

Figure 2 Schematic diagram of spout cells and sample cells.

Figure 3 Comparison of concentration values with error bar for ten repeats with literature values.

Figure 4 Typical flow pattern images.

Figure 5 Axial distribution of tracer concentration at different spouting gas flow rates. (a) in the spout cell 1; (b) in the spout cell 2; (c) in the spout cell 3.

Figure 6 Lateral distribution of tracer concentration at different spouting gas flow rates. (a) in the spout cell 1; (b) in the spout cell 2; (c) in the spout cell 3.

Figure 7 Schematic diagram of mixing mechanisms occurring at different flow structures.

Figure 8 Evolution of mixing index with time at different operation conditions.

Figure 9 Effect of central spouting gas flow rate on dimensionless mixing time.

Figure 10 Effect of auxiliary spouting gas flow rate on dimensionless mixing time.

Figure 11 Flow regime and mixing rate map.

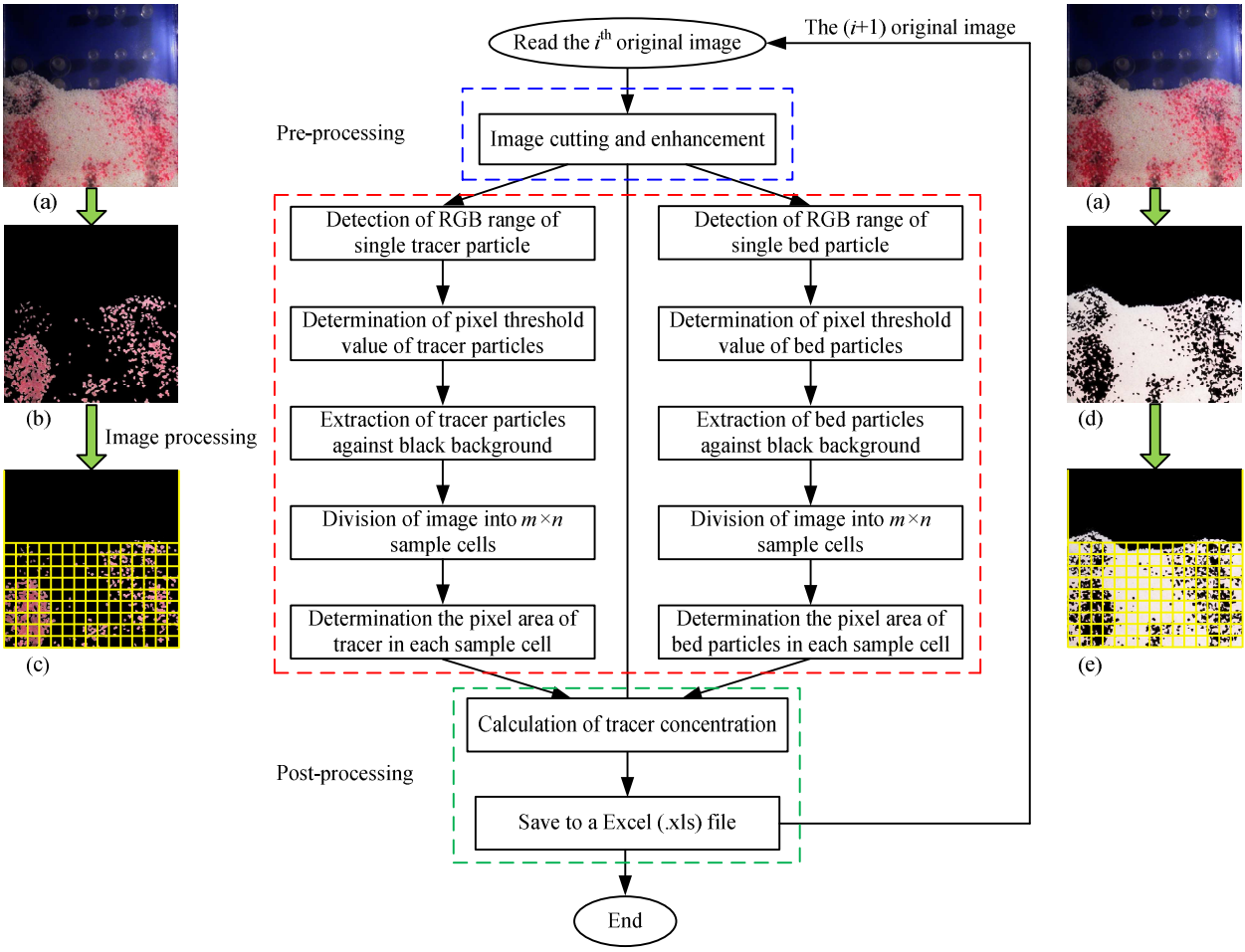

Figure 1 Flow chart of an image batch processing algorithm for calculating tracer concentration of a series of images. (a) original image; (b) detected tracers against the black background; (c) detected bed materials against the black background; (d) sample cell division for tracers; (e) sample cell division for bed materials.

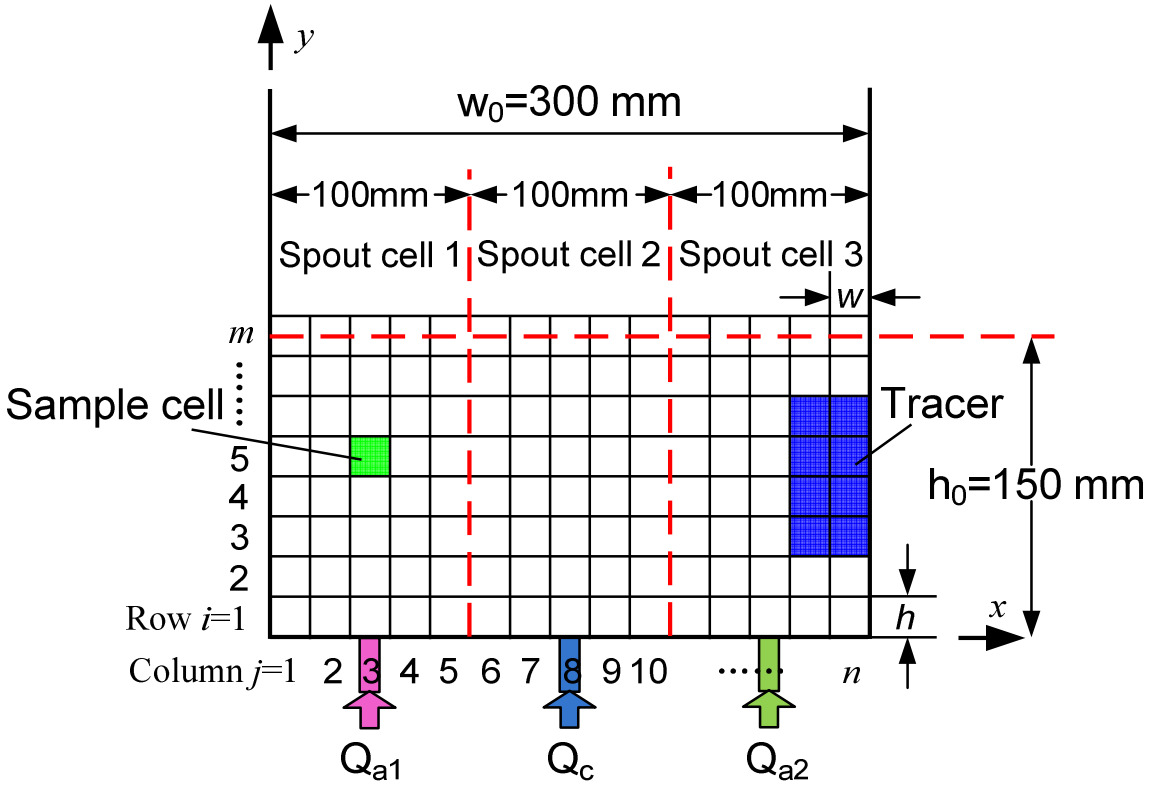

Figure 2 Schematic diagram of spout cells and sample cells.

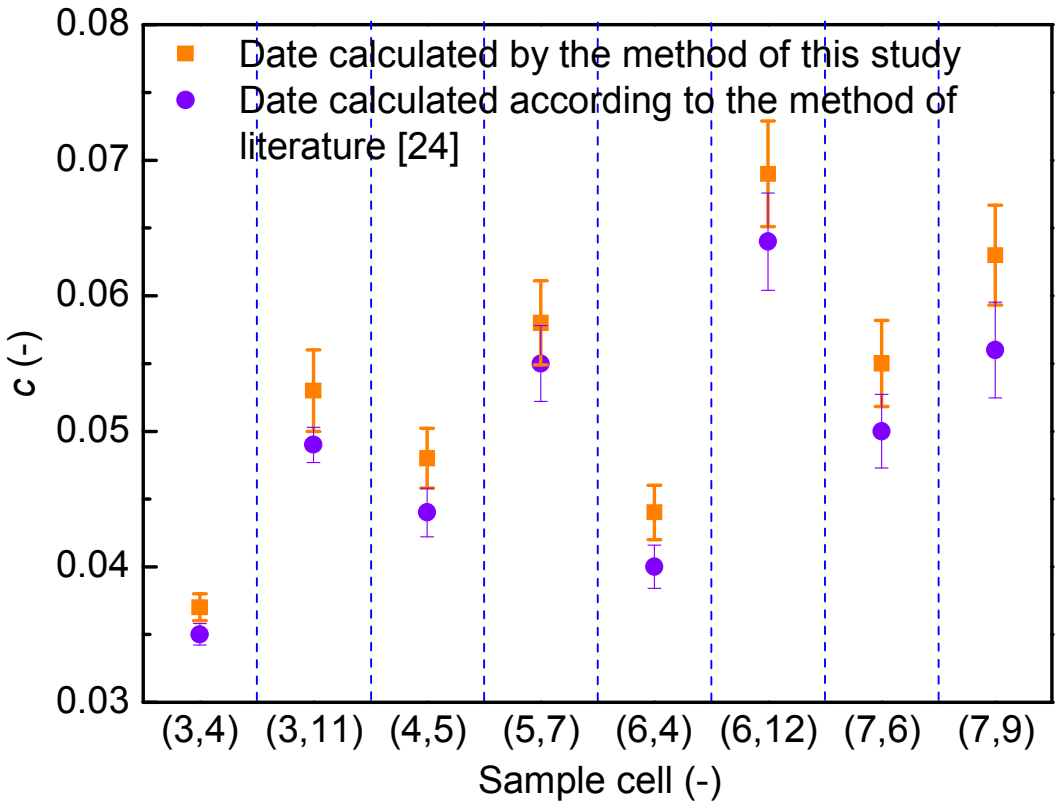

Figure 3 Comparison of concentration values with error bar for ten repeats with literature values.

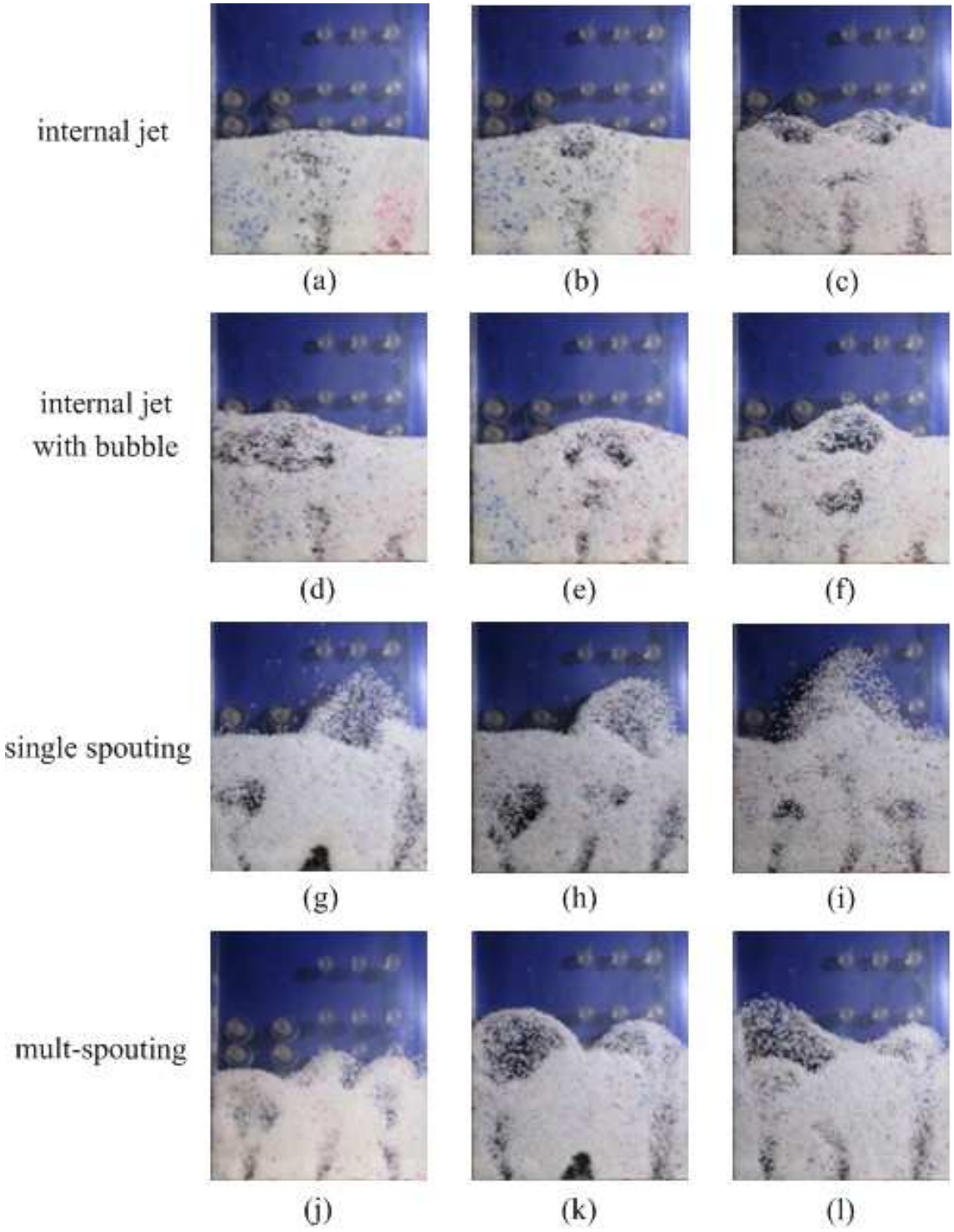

Figure 4 Typical flow pattern images.

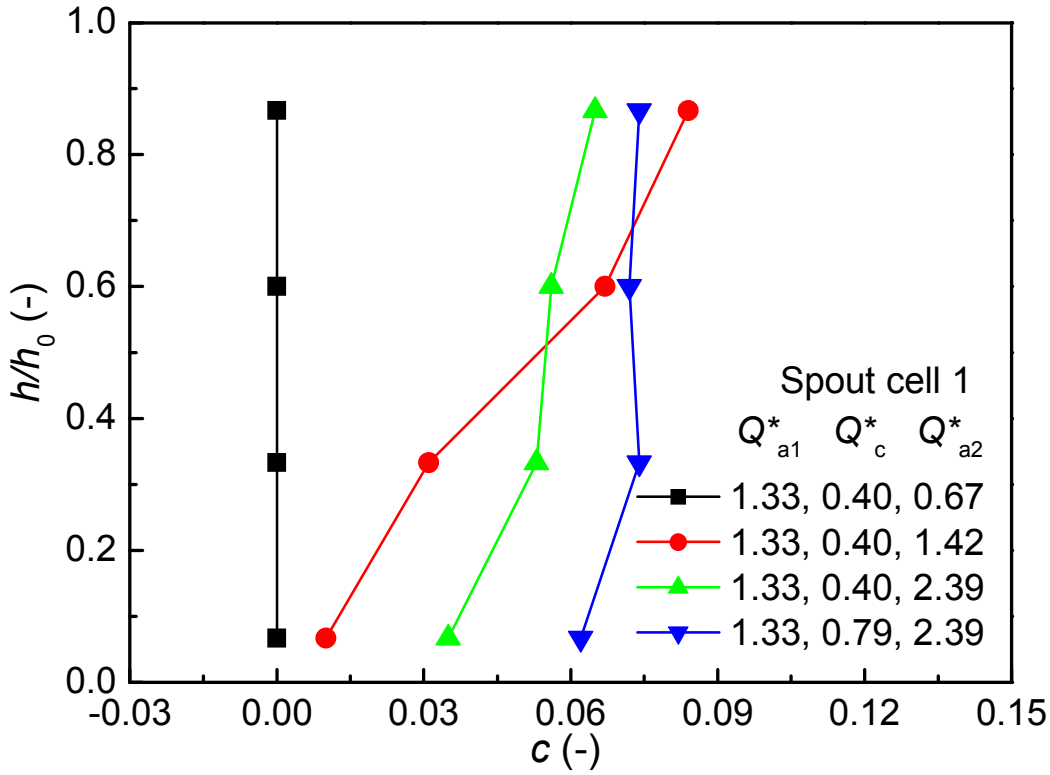
1.0
0.8
0.6
0.4
0.2
0.0
h/h0 (-)
-0.03
0.00
0.03
0.06
0.09
0.12
0.15
c (-)
Spout cell 1
Q*a1 Q*c Q*a2
1.33, 0.40, 0.67
1.33, 0.40, 1.42
1.33, 0.40, 2.39
1.33, 0.79, 2.39

(a)

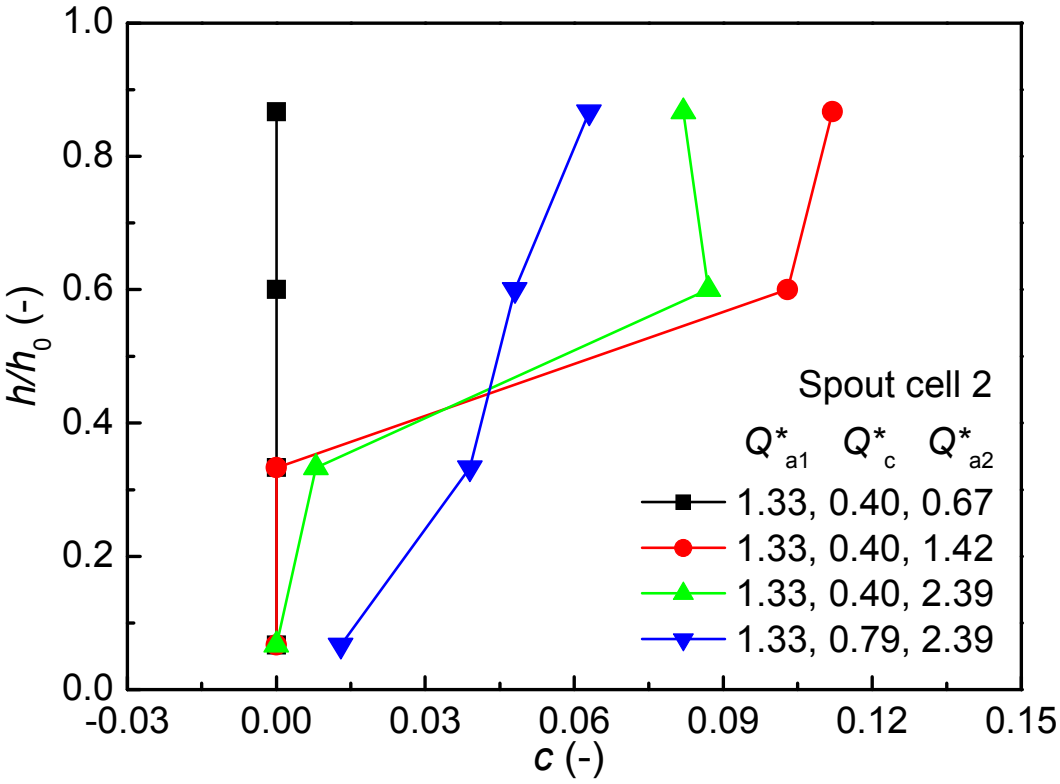
1.0
0.8
0.6
0.4
0.2
0.0
h/h0 (-)
-0.03
0.00
0.03
0.06
0.09
0.12
0.15
c (-)
Spout cell 2
Q*a1 Q*c Q*a2
1.33, 0.40, 0.67
1.33, 0.40, 1.42
1.33, 0.40, 2.39
1.33, 0.79, 2.39

(b)

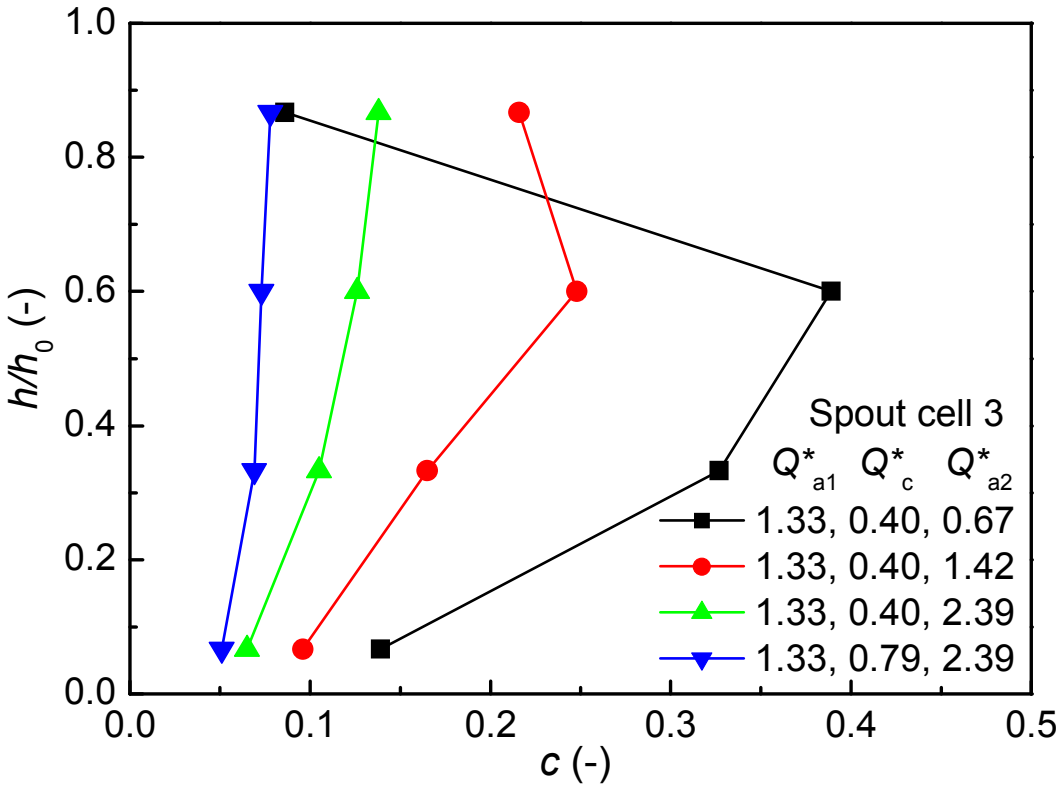

(c)

Figure 5 Axial distribution of tracer concentration at different spouting gas flow rates. (a) in the spout cell 1; (b) in the spout cell 2; (c) in the spout cell 3.

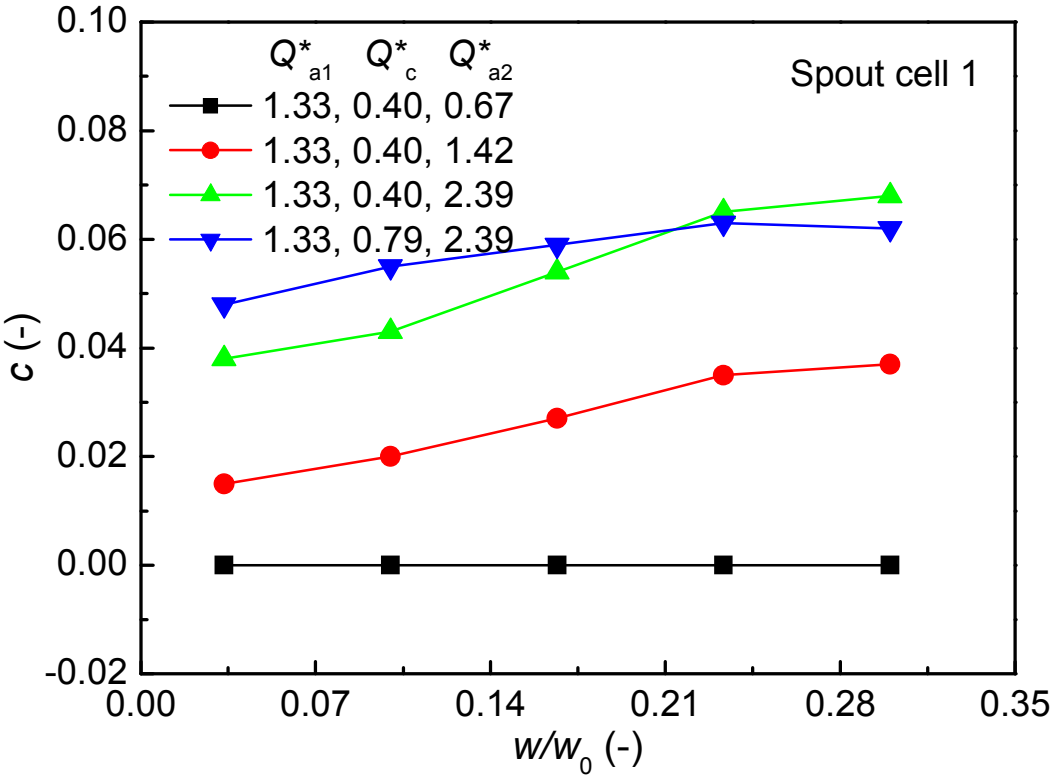
0.10
0.08
0.06
0.04
0.02
0.00
-0.02
c (-)
0.00
0.07
0.14
0.21
0.28
0.35
w/w0 (-)
Q*a1 Q*c Q*a2
1.33, 0.40, 0.67
1.33, 0.40, 1.42
1.33, 0.40, 2.39
1.33, 0.79, 2.39
Spout cell 1

(a)

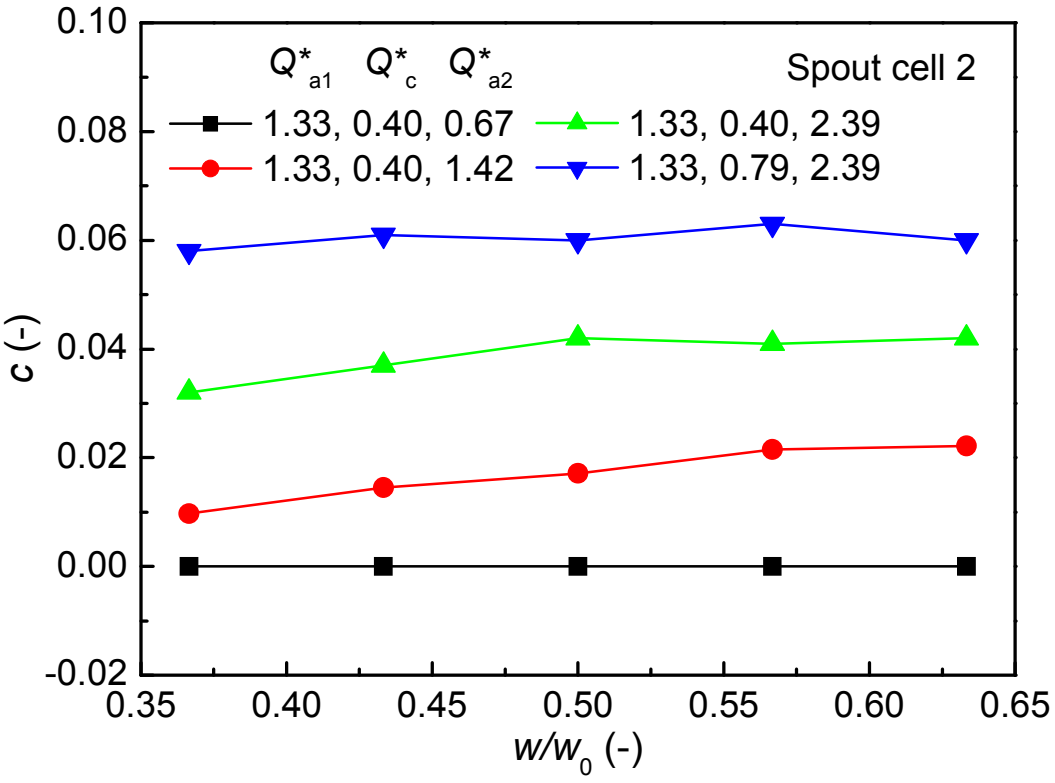
0.10
0.08
0.06
0.04
0.02
0.00
-0.02
c (-)
0.35
0.40
0.45
0.50
0.55
0.60
0.65
w/w0 (-)
Q*a1 Q*c Q*a2
Spout cell 2
1.33, 0.40, 0.67
1.33, 0.40, 2.39
1.33, 0.40, 1.42
1.33, 0.79, 2.39

(b)

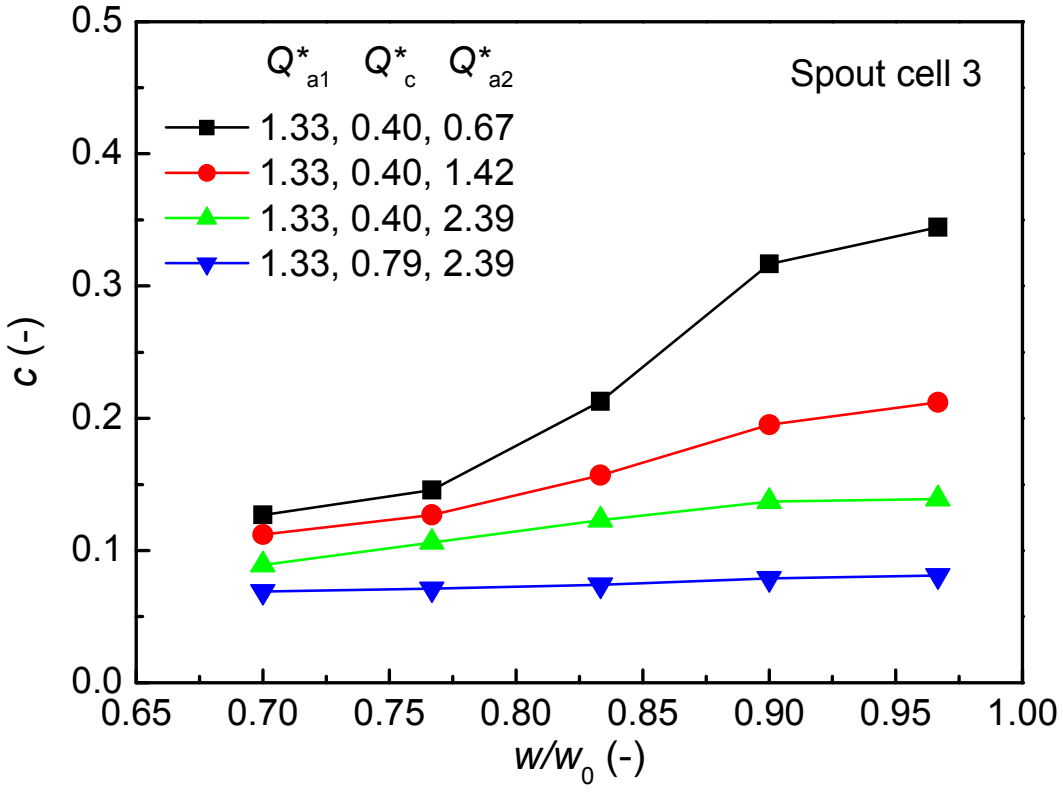

(c)

Figure 6 Lateral distribution of tracer concentration at different spouting gas flow rates. (a) in the spout cell 1; (b) in the spout cell 2; (c) in the spout cell 3.

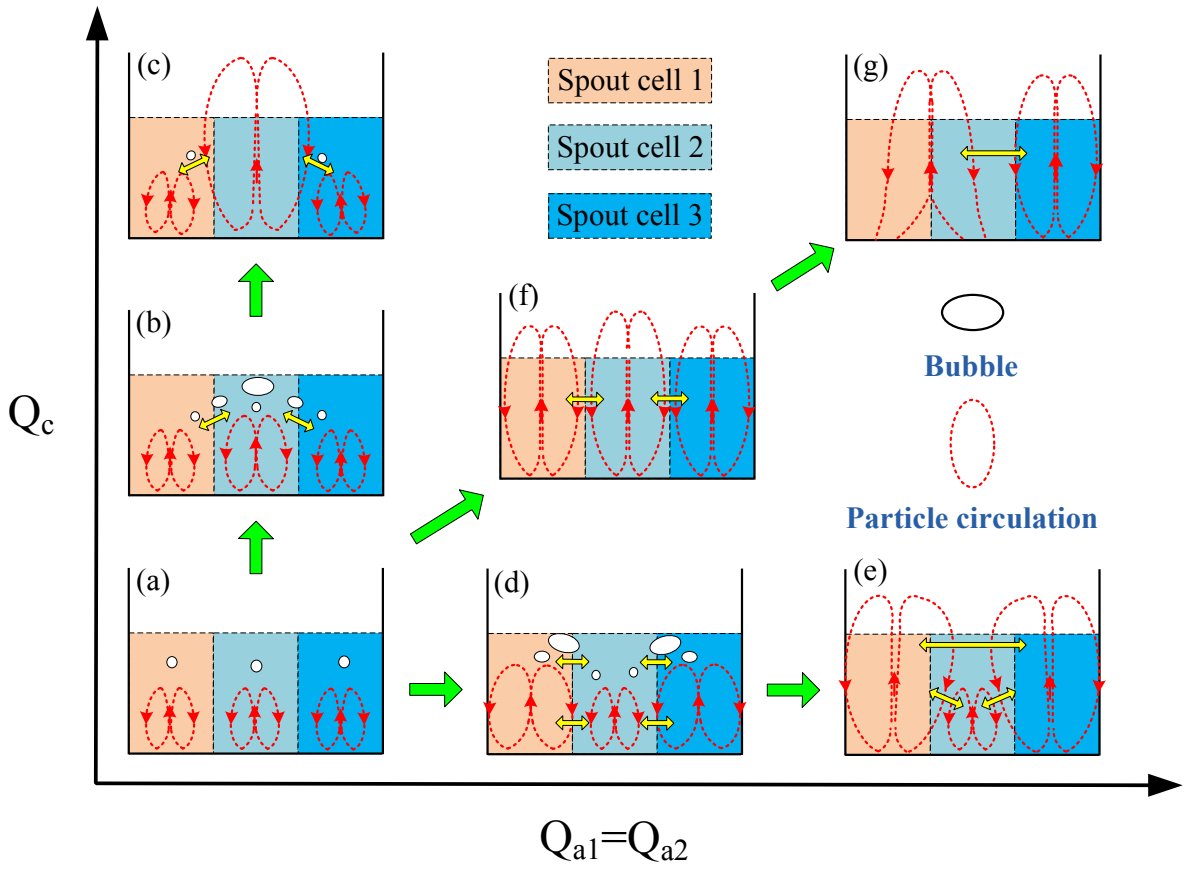

Figure 7 Schematic diagram of mixing mechanisms occurring at different flow structures.

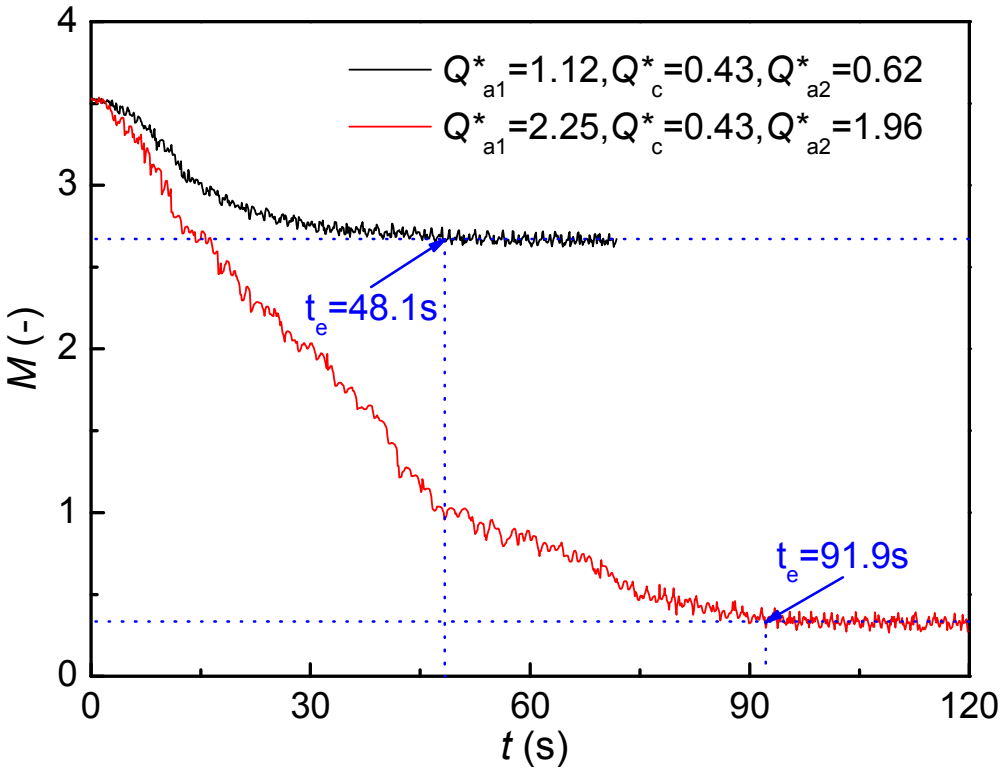

Figure 8 Evolution of mixing index with time at different operation conditions.

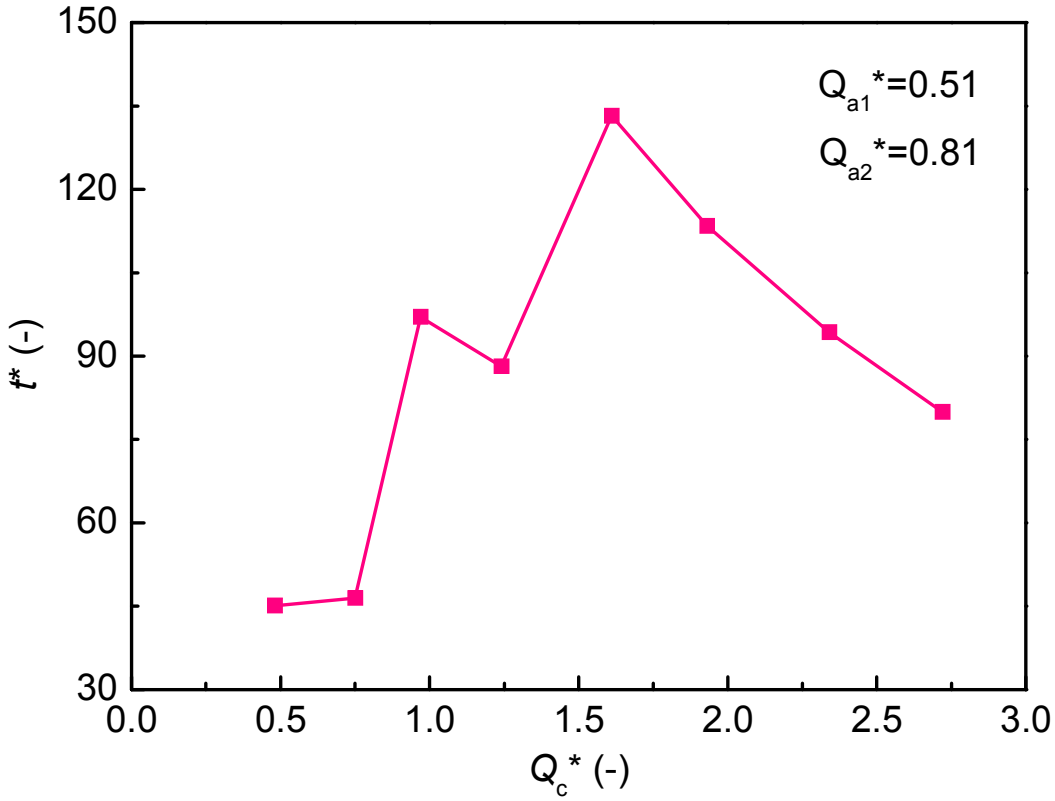

Figure 9 Effect of central spouting gas flow rate on dimensionless mixing time.

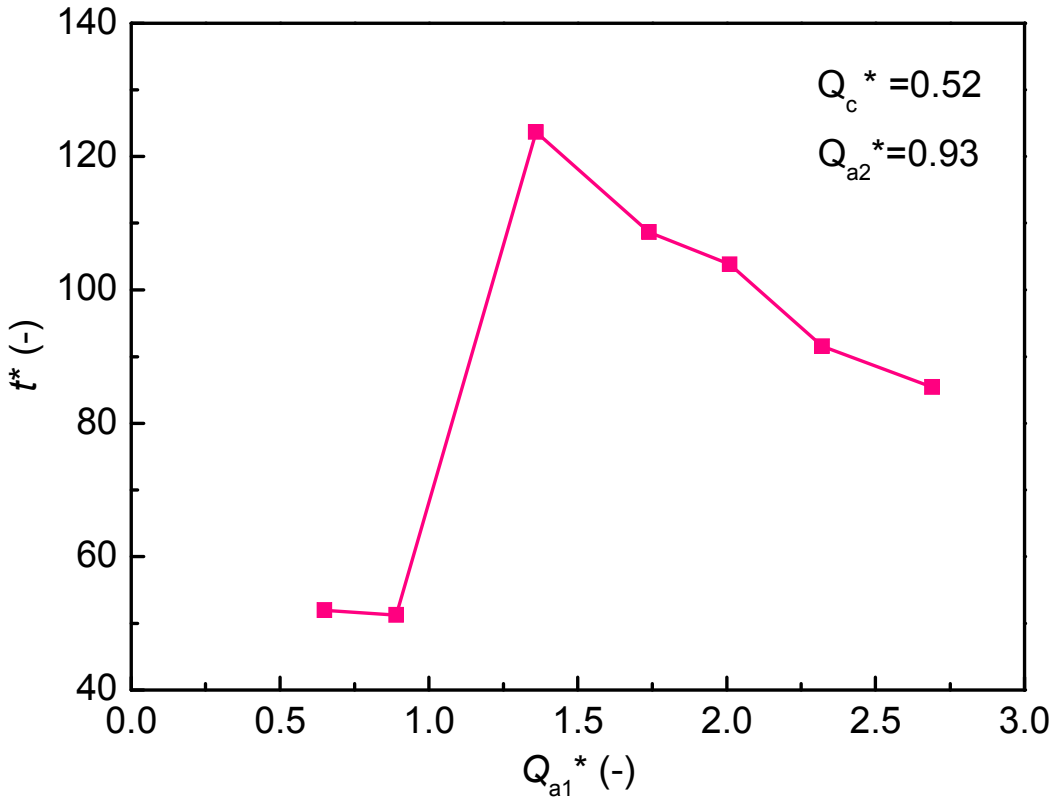

Figure 10 Effect of auxiliary spouting gas flow rate on dimensionless mixing time.

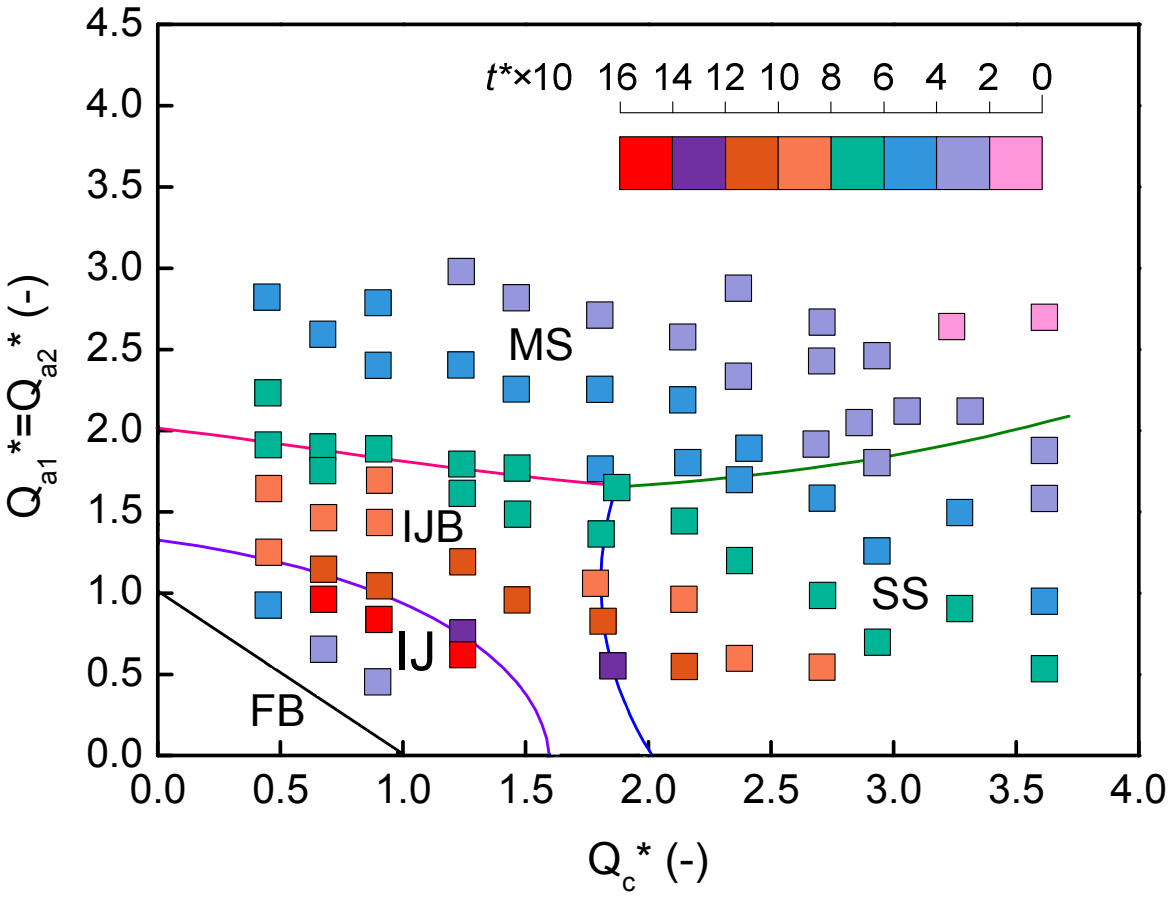

Figure 11 Flow regime and mixing rate map.